RSC Advances

PAPER

View Article Online
View Journal | View Issue

Cite this: *RSC Adv.*, 2026, **16**, 23101

Photothermal carbon black coatings enable efficient solar-driven membrane distillation

Mubark Alshareef,[a] Amr Mohamed Mahmoud,[b] Ahmed S. AL-Ghamdi,[b] Hesham Alhumade,[c] Ibrahim Mustafa,[c] Mohammed T. Alotaibi,[d] Ahmed Alharbi,[a] Bassant Ebraheem[e] and Mohamed E. A. Ali *[e]

Membrane distillation (MD) is a promising thermally driven desalination technology; however, its practical implementation remains limited by low vapor flux and pronounced temperature polarization. In this study, a thin photothermal coating composed of polyvinyl alcohol (PVA) and nanostructured carbon black (CB) was spray-deposited onto a commercial porous PTFE membrane to enhance solar-driven MD performance. The resulting PVA–CB layer exhibited strong broadband light absorption and efficient photothermal conversion in the visible-near infrared (Vis-NIR) range. Structural and optical analyses confirmed a turbostratic graphitic structure with a crystallite size of 36.3 nm, a microstrain of 3.44 × 10^{-4}, and an effective direct optical band gap of 3.58 eV determined from Tauc analysis of the dominant π–π^* transitions. Under simulated solar irradiation, the modified membrane showed a pronounced increase in surface temperature, enabling enhanced interfacial evaporation. Consequently, the PVA–CB membrane achieved a 45–60% increase in vapor flux compared with pristine PTFE, reaching up to 1.3 L m^{-2} h^{-1} at a temperature difference of 40 °C, while maintaining salt rejection above 99% and stable long-term operation. This improvement is attributed to the synergistic effects of CB-induced localized photothermal heating and PVA-enhanced surface hydrophilicity, which collectively reduce temperature polarization and facilitate efficient heat and mass transfer. These results highlight a scalable, cost-effective strategy for fabricating durable photothermal membranes, thereby advancing solar-driven desalination and sustainable water treatment.

Received 9th March 2026
Accepted 27th April 2026

DOI: 10.1039/d6ra02032a

rsc.li/rsc-advances

1. Introduction

Rapid population growth, accelerating industrialization, and the intensifying impacts of climate change have made freshwater scarcity one of the most pressing global challenges. Conventional desalination technologies, such as reverse osmosis and thermal distillation, are typically energy-intensive, costly, and susceptible to membrane fouling, which limits their long-term sustainability and large-scale deployment. Membrane distillation (MD) has emerged as a promising alternative because it can utilize low-grade or solar thermal energy and effectively treat high-salinity feedwaters.[1–3] Nevertheless, the practical performance of MD is often constrained by low vapor flux and severe temperature polarization at the membrane interface, resulting in reduced thermal efficiency and productivity. These limitations highlight the need for advanced photothermal materials capable of localizing heat at the membrane surface and enhancing mass-transfer efficiency. CB, owing to its strong broadband light absorption, high photothermal conversion efficiency, and low cost, represents an attractive candidate for addressing these challenges and enabling more energy-efficient MD systems.[4–6]

Carbon-based materials have attracted considerable interest in environmental, energy, and separation technologies due to their chemical stability and tunable surface chemistry. Among them, CB is distinguished by its turbostratic nanostructure, strong optical absorption, and efficient photothermal conversion capability.[7] Unlike diamond-like or amorphous carbon films, which are typically valued for their mechanical hardness and low friction, CB can rapidly localize heat under solar irradiation.[3,8,9] This property makes it particularly suitable for enhancing MD performance by improving surface heating, mitigating temperature polarization, and promoting efficient vapor generation. In addition, carbon-based matrices can serve as versatile hosts for functional nanostructures. While SiO_2 or Al_2O_3 supported composites have been widely investigated for

[a]*Department of Chemistry, Faculty of Science, Umm Al-Qura University, Makkah, Saudi Arabia*
[b]*Water Technologies Innovation Institute and Research Advancement, Jubail, Saudi Arabia*
[c]*Department of Chemical and Materials Engineering, Faculty of Engineering, King Abdulaziz University, Jeddah, 21589, Saudi Arabia*
[d]*Department of Chemistry, Turabah University College, Taif University, P. O. Box 11099, Taif, 21944, Saudi Arabia*
[e]*Egypt Desalination Research Center of Excellence (EDRC) & Hydrogeochemistry Dept., Desert Research Center, Cairo, 11753, Egypt. E-mail: m7983ali@gmail.com*

photonic applications, CB offers distinct advantages for photothermal-driven separation processes due to its strong light absorption and thermal localization properties.[3,9,10] A comprehensive understanding of CB across multiple length scales is essential because its structural features strongly influence its optical behavior, particularly in the ultraviolet region.[2,11] CB primary particles, typically ranging from a few nanometers to approximately 100 nm, consist of basic structural units (BSUs) composed of turbostratic graphitic domains. These domains comprise stacks of four to five or more graphene layers in which carbon atoms exhibit sp^2 hybridization, governing both bonding characteristics and optical properties. The presence of heteroatoms, such as oxygen, can further modify these electronic and optical properties. Therefore, precise characterization of these structural features is critical for the rational design of carbon-based nanocomposites.[12] Several theoretical models, including the Tauc,[3,13] Tauc–Lorentz (TL),[14] and Forouhi–Bloomer (FB)[15] models.have been employed to describe electronic transitions in amorphous carbon and related materials. However, their applicability to CB remains incompletely understood and requires further investigation.[16–18]

In recent years, MD has been increasingly explored for the desalination of high-salinity waters,[17,19] beverage concentration, produced-water treatment, and the separation of volatile compounds such as methanol and ammonia.[20–22] One of the principal advantages of MD is its relatively stable energy consumption across a wide range of feed salinities,[21] which makes it particularly compatible with renewable energy sources, especially solar power. Integrating MD with solar energy through photothermal coatings enables localized heating at the membrane–solution interface, thereby alleviating temperature polarization and enhancing permeate flux.[23–26] Light-absorbing materials, including CB, can be immobilized on membrane surfaces to harvest solar energy while preserving vapor-transport pathways, providing a scalable and cost-effective strategy for solar-driven desalination.[24,27,28] Despite these advantages, further improvements in MD efficiency and long-term operational stability are required for large-scale implementation. In particular, the development of low-cost, stable, and highly efficient photothermal coatings remains a critical challenge. Although CB has been explored as a photothermal material, systematic studies that directly correlate its structural and optical properties with desalination performance remain limited.[29–32]

In this work, PVA–CB nanocomposite coatings were deposited onto PTFE membranes *via* spray coating to enhance photothermal conversion and vapor flux in solar-driven MD. The optical, morphological, and structural properties of the coatings were systematically characterized, and their influence on desalination performance was evaluated. The novelty of this study lies in establishing a quantitative correlation between advanced optical parameters, including the Wemple–Di-Domenico oscillator model, volume and surface energy loss functions (VELF/SELF), and nonlinear optical constants, and the resulting photothermal desalination efficiency. By linking these parameters to the electronic structure and optical band gap of CB the study provides fundamental insight into interfacial heating and energy loss mechanisms at the membrane surface. Unlike prior MD studies that focus primarily on empirical performance metrics or material screening, this work introduces a predictive, physics-based framework that connects optical properties with photothermal behavior. This integrated approach bridges the gap between optical materials science and membrane distillation engineering, enabling the rational design of efficient, durable, and scalable photothermal membranes for solar-driven water treatment applications.

2. Experimental

2.1. Materials

The CB nanopowder was purchased from US Research Nanomaterials, Inc (Houston, USA), and has an average particle size of approximately 150 nm. Poly(vinyl alcohol) (PVA; molecular weight 85 000–124 000, 95.5–96.5% hydrolyzed) was obtained from ACROS Organics, while glutaraldehyde (GA; 50% aqueous solution) was supplied by ADWIC. The PVA/CB layer was fabricated on a hydrophobic polytetrafluoroethylene (PTFE) membrane supported by polypropylene (PP) with a pore size of 0.45 μm, supplied by Jian City Qing Feng Filter Equipment Co., Ltd. Acetone, ethanol, and hydrochloric acid (36–37%) were purchased from PIOCHEM. Salt test solutions ($MgSO_4 \cdot 7H_2O$, Na_2SO_4, NaCl, $NaHCO_3$, $CaCl_2$, and KCl) were prepared using deionized water produced by a LUNDA PD 8 R system (Germany). All chemicals were used as received without further purification.

2.2. Preparation of the PVA-CB/PTFE composite membrane

2.2.1. Preparation of CB thin films for optical characterization. For optical property measurements, pure CB thin films were prepared on highly transparent quartz substrates by dispersing 0.05 g of CB nanopowder in 2 mL of ethanol, followed by spray coating using the same equipment at 50 psi. The coated quartz substrates were dried in an oven at 100 °C for 15 min to remove residual solvent and enhance film adhesion.

2.2.2. Preparation of the coated membranes. PVA solutions (1.0–1.5 wt%) were prepared by dissolving the PVA powder in a water/ethanol mixture (2 : 3 v/v) at 90 °C under continuous stirring for 2 h until complete dissolution. CB was subsequently added at concentrations of 0.75 or 1.0 wt%, and the mixtures were sonicated for 1 h to ensure homogeneous dispersion. The resulting PVA–CB composite solutions were degassed to remove air bubbles before use. Prior to spray coating deposition of the PVA–CB solution, the PTFE membrane was gently pre-wetted with 5 mL of ethanol to clean the surface and mildly enhance wettability, thereby improving adhesion of the PVA–CB layer without causing deep penetration into the hydrophobic pores. Then the PVA–CB solution was deposited onto the pre-treated PTFE substrate using a Master Airbrush (Model G22) connected to a 1/5 HP air compressor operating at a constant pressure of 50 psi. Multiple controlled overlapping passes were applied to achieve a thin and uniform surface layer. After deposition, the membranes were allowed to air-dry at room

temperature for 10 min. After that, crosslinking was carried out by spraying a solution containing 2 wt% GA in a 2 : 3 (v/v) acetone/water mixture, catalyzed with 0.12 mol L^{-1} HCl. The membranes were then dried overnight at room temperature. Subsequently, the crosslinked films were thoroughly washed with ethanol and distilled water to remove residual GA and HCl, ensuring the removal of any uncrosslinked hydrophilic material. The final membranes were stored at room temperature until further characterization and testing.

To mitigate the risk of pore wetting associated with the hydrophilic PVA component, several precautions were implemented. The PTFE substrate was only mildly pre-wetted with ethanol, and the PVA–CB solution was sprayed at controlled low pressure to restrict deposition to the membrane surface. The GA crosslinking step fixed the PVA network, rendering it insoluble and mechanically stable on the top surface while preserving the hydrophobicity of the underlying PTFE layer. Thorough post-washing effectively eliminated any loose hydrophilic residues.[1–3] Fig. 1 illustrates the fabrication process of the PVA–CB/PTFE composite photothermal membrane.

2.3. Characterization

Detailed characterization of the materials and membranes, as well as photothermal experiments is provided in the SI.

2.3.1. Optical properties of CB thin film. The optical properties of the prepared CB thin films were characterized using a JASCO V-670 UV-Vis-NIR spectrophotometer operated in a dual-beam configuration. Measurements were performed at normal incidence over a wide spectral range of 200–2500 nm. High-precision optical transmittance, $T(\lambda)$, and reflectance, $R(\lambda)$, spectra were recorded to investigate the interaction of light with the thin films. To determine the key optical constants—namely the refractive index (n), absorption coefficient (α), and extinction coefficient (k)—a dedicated computational program was employed. This software analyzed the absolute reflectance and transmittance data, $R(\lambda)$ and $T(\lambda)$, to extract the wavelength-dependent optical parameters. The absorption coefficient α was calculated using the relation reported in ref. 4 and 5.

$$\alpha = \frac{1}{d}\ln\left[\left(\frac{(1-R)^2}{2T}\right) + \left(\left(\frac{(1-R)^4}{4T^2}\right) + R^2\right)^{\frac{1}{2}}\right] \quad (1)$$

$$k = \frac{\alpha\lambda}{4\pi} \quad (2)$$

$$n = \left(\frac{4R}{(1-R)^2} - K^2\right)^{\frac{1}{2}} + \left(\frac{1+R}{1-R}\right) \quad (3)$$

The absolute values of R and T are given by the following equation, where the film's deposited thickness is.

$$T = \left(\frac{I_{ft}}{I_q}\right)(1 - R_q) \quad (4)$$

$$R = \left(\frac{I_{ft}}{I_m}\right)R_m\left(1 + \left[1 - R_q\right]^2\right) - T^2R_q \quad (5)$$

To ensure accurate determination of the optical parameters, the measurements were analyzed using a computational method based on Murmann's precise equation. This approach accounted

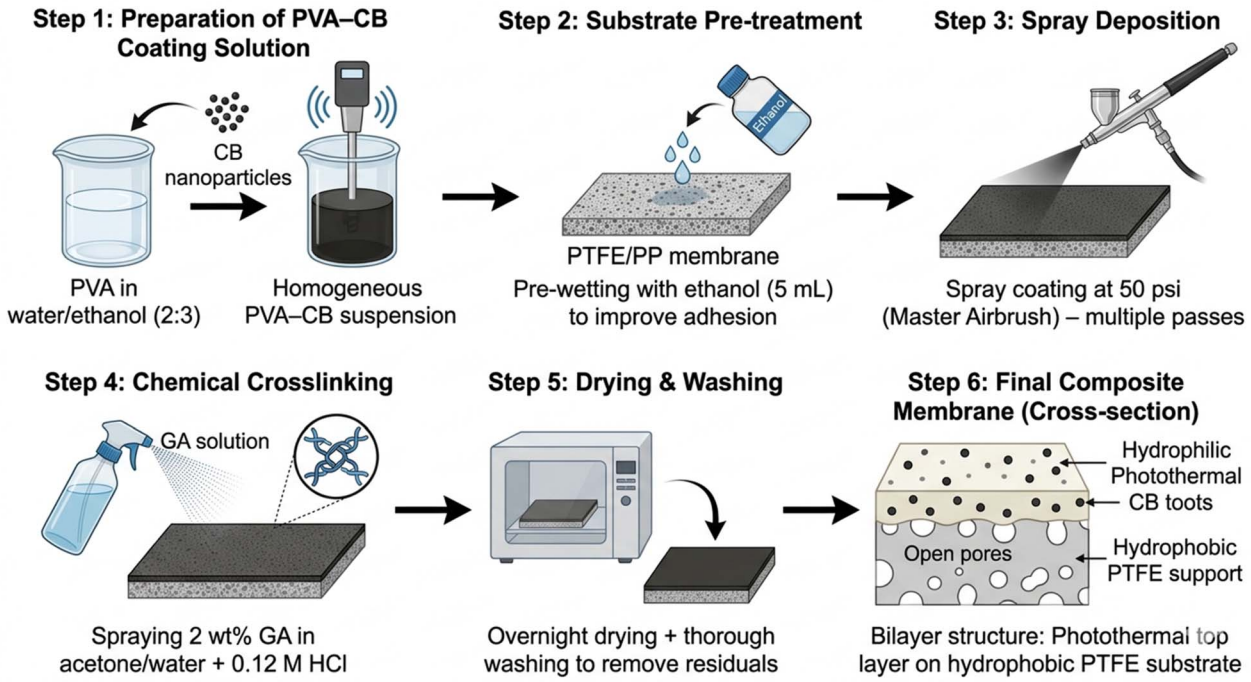

Fig. 1 A schematic diagram illustrating the step-by-step fabrication of the PVA–CB/PTFE composite photothermal membrane *via* spray-coating technique.

for several experimentally measured quantities. Specifically, I_{ft} represents the intensity of light transmitted through the film–quartz structure. R_q denotes the reflectance of the quartz substrate, while I_q refers to the reflected light intensity from the bare quartz substrate. In addition, I_m is the reference light intensity reflected from a standard mirror with a known reflectance R_m. These measured intensities formed the basis for the precise determination of the reflectance and transmittance of the thin-film samples. Experimental uncertainties were carefully evaluated to ensure the reliability of the derived optical parameters. The uncertainty in film thickness measurements was assumed to be within ±3%, whereas the uncertainties in reflectance $R(\lambda)$and transmittance $T(\lambda)$were estimated to be within ±1%. As a result, the calculated extinction coefficient k and refractive index n were associated with an overall uncertainty of approximately ±3%. This level of precision confirms that the extracted optical constants reliably represent the intrinsic optical behaviour of the CB thin films under investigation.

The optical band gap (E_g) of the CB film was determined using Tauc's relation, This relationship is expressed by the following eqn (6) and (7):

$$(\alpha E)^2 = A(E - E_g) \tag{6}$$

The optical dispersion of the CB thin film was analysed using the Wemple–DiDomenico single-oscillator model,[8]

$$\left(n^2 - 1\right)^{-1} = \frac{E_o}{E_d} - \frac{1}{E_o E_d}E^2 \tag{7}$$

Analysis of the n^2 *versus* λ^2 relationship (eqn (10)) yielded a lattice dielectric constant (ε_L) and a high carrier concentration-to-effective-mass ratio (N/m^*).

$$\varepsilon_1 = n^2 = \varepsilon_L - \frac{e^2 N}{4\pi^2 \varepsilon_o m^* C^2}\lambda^2 \tag{8}$$

The complex dielectric function, $\varepsilon(E)$, governs the optical response of materials, including transmission, reflection, and absorption, and is essential for optoelectronic device design. It is defined as;

$$\varepsilon(E) = \varepsilon_1(E) + i\varepsilon_2(E) \tag{9}$$

where $\varepsilon_1(E)$ and $\varepsilon_2(E)$ are the real and imaginary parts, respectively. These quantities are related to the refractive index (n) and extinction coefficient (k) by;

$$\varepsilon_1(E) = n^2 - k^2 \text{ and } \varepsilon_2(E) = 2nk \tag{10}$$

The interaction of incident electromagnetic radiation with electrons in a material can be quantified using the Volume Energy Loss Function (VELF) and the Surface Energy Loss Function (SELF). These functions provide insights into the energy dissipated by electrons as they interact with the electromagnetic field at the surface and within the bulk of the material, respectively. Mathematically, SELF and VELF are related to the complex dielectric function, $\varepsilon(E) = \varepsilon_1(E) + i\varepsilon_2(E)$, *via* the following expressions:

$$\text{VELF} = -\text{Im}\left(\frac{1}{\varepsilon^*}\right) = \frac{\varepsilon_2}{{\varepsilon_1}^2 + {\varepsilon_2}^2} \tag{11}$$

$$\text{SELF} = -\text{Im}\left(\frac{1}{\varepsilon^* + 1}\right) = \frac{\varepsilon_2}{\left(\varepsilon_1 + 1\right)^2 + {\varepsilon_2}^2} \tag{12}$$

The study of nonlinear optics (NLO) is paramount for the development of advanced optoelectronic devices, including photosensitive signal processing units and optical switches. The nonlinear optical characteristics of CB-based devices are crucial for their successful implementation in these applications. The nonlinearity of a material is manifested through its polarization, which is related to the linear optical susceptibility ($\chi^{(1)}$), electric field (E), and second-order susceptibility ($\chi^{(2)}$) through the following eqn (9):

$$p = \chi^{(1)}E + \chi^{(2)}E^2 + \chi^{(3)}E^3 \tag{13}$$

To understand the nonlinear optical behavior of the CB thin film, the single oscillator parameters, oscillator energy (E_0) and dispersion energy (E_d), are correlated to $\chi^{(1)}$ *via* the following eqn (9):

$$\chi^{(1)} = \frac{(n^2 - 1)}{4\pi} \tag{14}$$

So

$$\chi^{(1)} = \left[\frac{E_o E_d}{4\pi\left({E_o}^2 - (h\nu)^2\right)}\right] \tag{15}$$

The third-order nonlinear susceptibility, $\chi^{(3)}$, is then calculated using the above equation, which relates it to $\chi^{(1)}$ and the static refractive index (n_0). The static refractive index, n_0, is obtained from the refractive index at zero photon energy ($h\nu \approx 0$) using the following eqn (10):

$$\chi^{(1)} = \frac{({n_o}^2 - 1)}{4\pi} = \frac{E_d}{4\pi E_o} \tag{16}$$

Furthermore, the photon energy dependence of $\chi^{(3)}$ is estimated using Miller's generalized rule and the Wemple–DiDomenico single oscillator model, as described by the following eqn (10):

$$\chi^{(3)} = A\left(\chi^{(1)}\right)^4 = A\left[\frac{E_o E_d}{4\pi\left({E_o}^2 - (h\nu)^2\right)}\right]^4 \tag{17}$$

3. Results and discussion

3.1. Structural and morphological investigation of CB

The XRD pattern of CB powder shown in Fig. 2A displays a broad diffraction feature centered at approximately $2\theta \approx 24$–

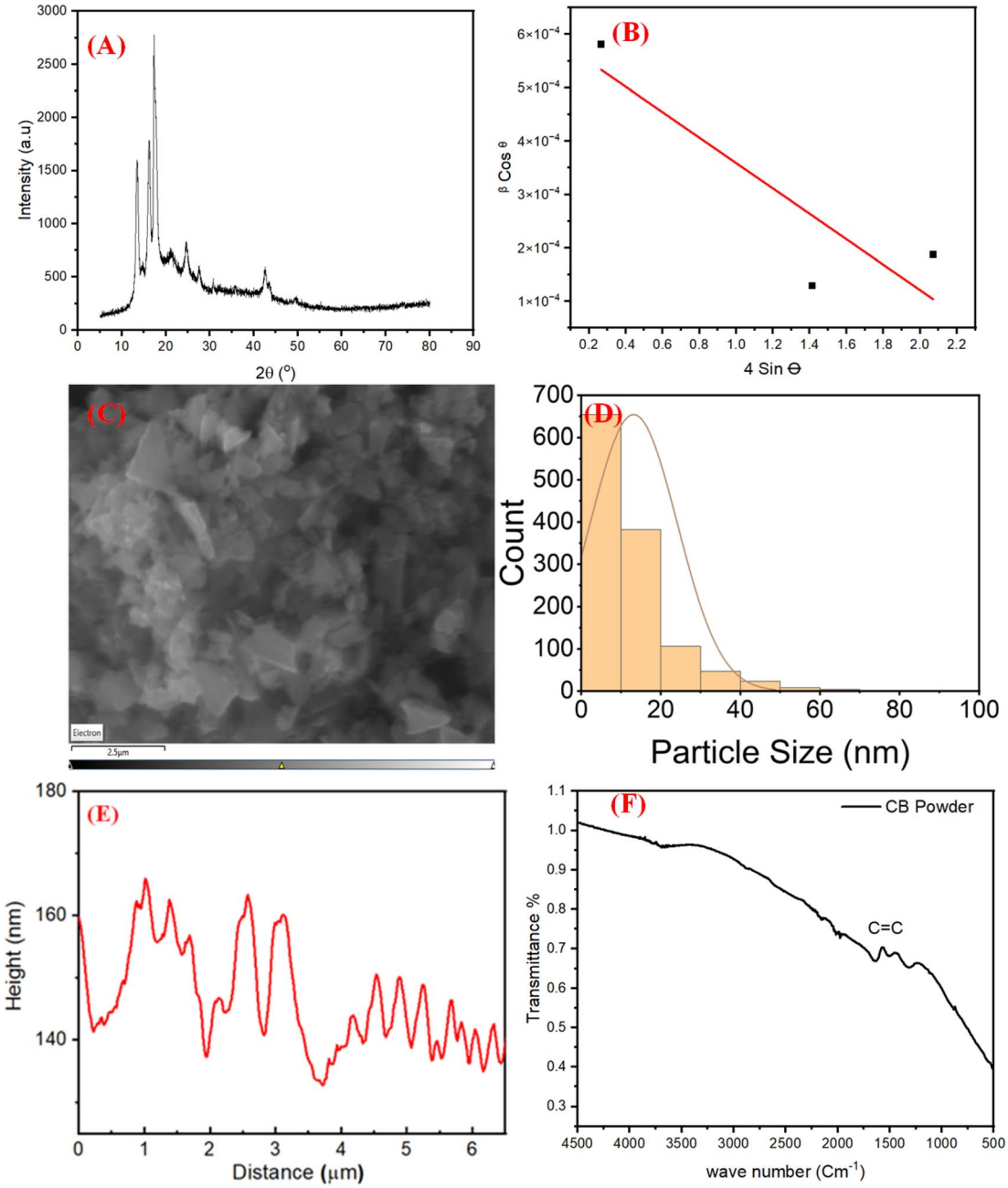

Fig. 2 XRD pattern of CB in powder form (A). The relation between ($\beta \cos \theta$) and (4 sin θ) (B). The front view of SEM images (C). The grain size distribution for CB (D). Height *vs.* distance of CB sample (E). FTIR spectrum of pure CB (F).

25°, corresponding to the (002) reflection of turbostratic graphitic domains with disordered interlayer stacking which is characteristic of disordered stacking of sp^2 carbon layers and reflects significantly reduced interlayer coherence compared with crystalline graphite. A weaker, broader band around 43–45° arises from the (10) in-plane reflections (overlapping 100 and 101). These characteristics are typical of CB, which consists of small, randomly oriented graphene-like stacks (turbostratic structure) rather than highly ordered graphite (sharp (002) at 26.5°). The absence of sharp peaks confirms the predominance of amorphous and turbostratic phases with limited long-range order suggests extremely small coherent scattering domain sizes (on the nanometer scale) and/or the presence of substantial microstrain and stacking disorder.[11] The average crystallite size (D) was estimated using the Williamson–Hall (W–H) method. This approach employs the simplified integral breadth of the diffraction peaks and evaluates peak broadening as a function of the diffraction angle (2θ).[8]

Fig. 2B illustrates the correlation between $\beta \cos \theta$ and 4 sin θ for all CB preferred turbostratic graphite-like structure. The strong linearity of the fitted data confirms homogeneous lattice distortion and uniformity of the crystalline planes. The analysis reveals a crystallite size of 36.3 nm and a microstrain value of 3.44×10^{-4} with a negative slope indicating compressive strain

due to structural defects and turbostratic disorder. The points exhibit reasonable linearity considering the heterogeneous nature of CB; deviations arise from anisotropic strain and size distribution common in turbostratic carbons.[8,11,12] The average dislocation density was determined to be 3.9×10^9 cm^{-2} reflecting significant lattice imperfections consistent with CB's nanostructured morphology. This relatively high value indicates the presence of significant structural imperfections and lattice disorder within the CB nanopowder, consistent with its turbostratic nature and the existence of nanocrystalline domains embedded in an amorphous matrix. The observed negative slope is particularly significant, as it denotes compressive behavior, in contrast to the positive slope typically associated with tensile strain. This compression suggests a reduction in lattice parameters relative to ideal graphitic structure, which may arise from structural defects or residual stresses introduced during the growth process. The nanoscale crystallite size indicates a limited domain structure, which directly influences the film's mechanical stability and optoelectronic properties. Although the measured microstrain appears moderate, its impact on key material characteristics, such as band-gap modulation, defect-state density, and charge-carrier dynamics, can be substantial. Internal strain plays a critical role in tailoring the functional performance of thin-film materials.[13–15]

The surface topography of the CB films was further analyzed using SEM images in combination with image-processing software. The front-view SEM image shown in Fig. 2C reveals a high grain density with pronounced clustering and a random spatial distribution across the surface, also; exhibit the characteristic morphology of branched aggregates with lateral dimensions reaching the micrometer scale. While the scale bar indicates features around 2.5 μm, these represent secondary aggregates or large clusters formed by the physical entanglement of carbon primary units. Fig. 2D presents the grain-size distribution and the corresponding line-profile produced from SEM image analysis. Based on the line-profile data, the average surface grain size was extracted, and it reveals that the primary particles (nodules) possess much smaller diameters, typically ranging from 10 to 40 nm. This hierarchical arrangement is typical for CB, where fused primary particles forming aggregates, which then associate into the larger micrometer-sized agglomerates observed in SEM. The nanometric size of these primary nodules is the key factor contributing to the high specific surface area and the reinforcing capabilities of the material in practical applications.[16] Interestingly, localized regions analyzed in Fig. 2E revealed grain sizes as small as approximately 5 nm. Such spatial variations suggest a non-uniform distribution across the surface, which is consistent with the random spatial distribution observed in the SEM front-view. The FTIR spectra of pure CB reveal the characteristic functional groups, as illustrated in Fig. 2F. The FTIR spectrum of pure CB is predominantly composed of amorphous carbon and lacks diverse functional groups. A weak and broad band around 1600 cm^{-1} is attributed to C=C stretching vibrations of aromatic domains within the carbon structure. Additionally, a minor band near 3400 cm^{-1} may indicate the presence of surface hydroxyl groups (–OH) or adsorbed moisture on the carbon particles.

3.2. Optical properties of CB thin film

3.2.1. Transmittance and reflectance characteristics of the CB thin film. Fig. 3 presents the optical spectral response of a CB thin film (coated on quartz) over a broad wavelength range, highlighting its strong wavelength-dependent interaction with light. Two optical parameters are shown corresponding to reflectance (red) and transmittance (black), plotted against wavelength from the ultraviolet (UV) to the near-infrared (NIR) region. Fig. 3 elucidates that at short wavelengths in the UV region, the CB film exhibits very low transmittance, accompanied by relatively high reflectance. This behavior indicates strong optical losses dominated by absorption, which is characteristic of carbon-based materials with a high density of electronic states and π–π^* electronic transitions. The sharp decrease in transmittance in the UV region suggests that incident photons are efficiently absorbed by the CB network rather than transmitted through the film. This confirms the well-known role of CB as an effective UV absorber. As the wavelength increases from the UV toward the visible region, the transmittance gradually increases, while the reflectance decreases. This transition reflects a reduction in absorption losses and a change in the balance between scattering, reflection, and absorption mechanisms. In the visible range, the film remains weakly transmissive, consistent with the intrinsic black appearance of CB, which absorbs a significant fraction of visible light. However, the gradual rise in transmittance indicates partial transparency at longer wavelengths, likely influenced by film thickness, particle dispersion, and porosity.

Overall, the figure demonstrates that CB thin films are highly absorptive in the UV and visible regions, with limited transmittance and moderate reflectance, while exhibiting increased reflectance in the NIR. These optical characteristics make CB particularly suitable as a solar thermal absorber for photothermal application in MD systems. The spectral trends also provide insight into the electronic structure and light–matter interaction mechanisms in CB, which are strongly influenced by its nanostructured morphology and degree of graphitization.[17]

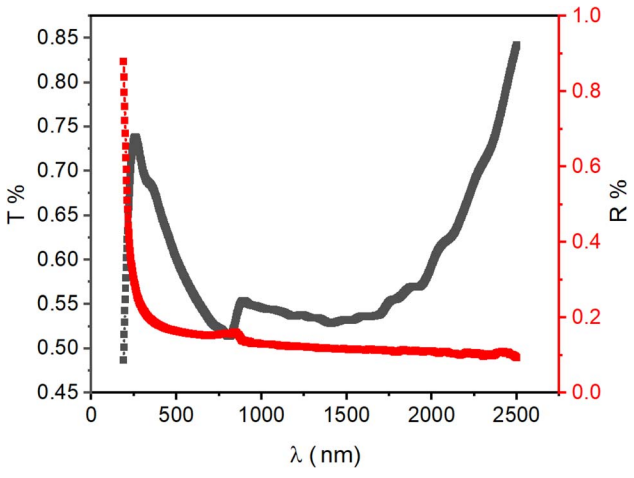

Fig. 3 Transmittance (T) and reflectance (R) as a function of incident wavelength (λ) across the 200–2500 nm range.

Fig. 4a illustrates the spectral dependence of the refractive index, $n(\lambda)$, and the extinction coefficient, $k(\lambda)$, of a CB film over the wavelength range of 200–2500 nm. The observed profiles of $n(\lambda)$ and $k(\lambda)$ are governed by the electronic band structure of the material and its interaction with incident light. In the UV region (200–400 nm), the refractive index exhibits a pronounced peak, indicating the presence of a resonance effect or an absorption band associated with electronic transitions within the CB structure. This sharp feature reflects strong optical dispersion, signifying a substantial wavelength-dependent variation in the refractive index within this spectral region. As the wavelength extends into the visible and NIR regions, the refractive index initially decreases, reaching a minimum around 1000 nm, followed by a gradual increase and eventual saturation at longer wavelengths. In contrast, the extinction coefficient, $k(\lambda)$, shows a monotonic increase with increasing wavelength, indicating enhanced optical absorption in the NIR region compared to the UV-visible range. This behavior suggests that the material becomes progressively more absorptive at longer wavelengths.

The optical band gap (E_g) of the CB film was determined using Tauc's relation, a widely accepted approach for correlating photon energy ($h\nu$) with the absorption coefficient (α) in semiconductor materials, particularly within the high-absorption regime. The relationship between $\alpha h\nu^2$ and photon energy (E) is linear in the vicinity of the absorption edge, which enables direct determination of the optical band gap (E_g). From Fig. 4b, the extrapolation of the linear region of the curve to the energy axis intercept yields the direct optical band gap. This approach is based on the principle that electronic transitions near the band edge govern the observed absorption behaviour. The extracted band gap value of 3.58 eV for the CB film represents a fundamental material property that strongly influences its suitability for photothermal applications. The experimentally determined band gap of 3.58 eV for the CB film reported in this study falls within the range of values previously reported in the literature,[10,18,19] although considerable variation has been observed. As summarized in Table 1, reported E_g values for CB span from approximately 4.0 to 5.1 eV, reflecting a strong dependence on synthesis conditions, structural characteristics, and the presence of dopants or surface modifications. For example, pristine CB films have been reported to exhibit higher band gap values of up to 5.1 eV.[18,20]

3.2.2. Refractive index and dispersion characteristics of the CB film. The optical dispersion of the CB thin film was analysed

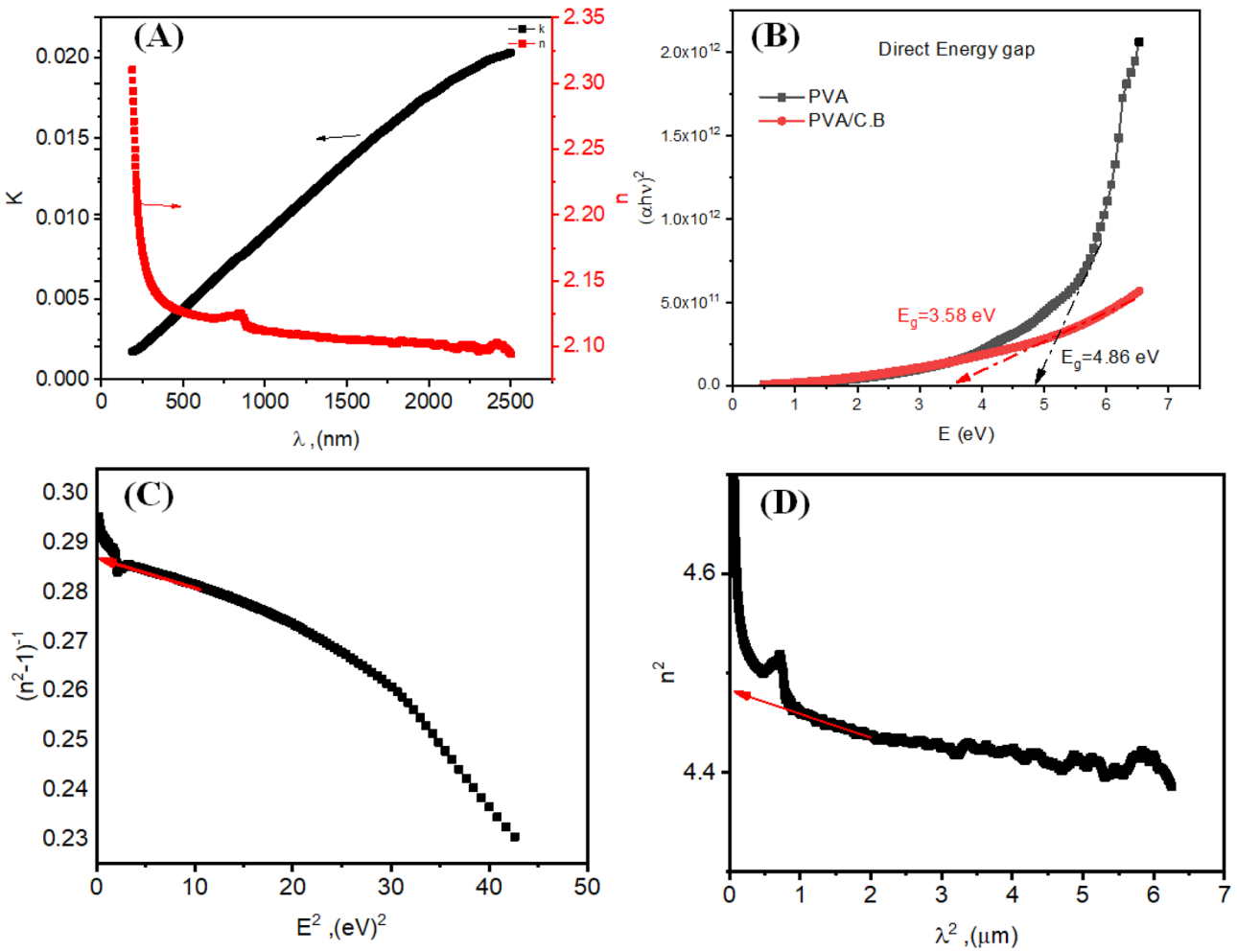

Fig. 4 Plot of spectral depends of refractive index n (λ), (Right side) and absorption index $K(\lambda)$, (Left side) (A), and plot of $(\alpha h\nu)^2$ *versus* E (B), plot of $(n^2-1)^{-1}$ *versus* $(E)^2$ (C), and plot of n^2 as a function of λ^2 (D) of CB in PVA film.

Table 1 Energy gap of the CB thin film compared with values reported in the literature

Samples	E_g (eV)	References
Polyester-carbon black (3–12%)	5.1–4.9	20
CNPs	1.2 ± 0.1^a	21
Nanocluster carbon thin films	3.62, 3.77	22
PEO doped with 0.1 wt% carbon black	4.02	23
PANI/NC	2.1	24
CS/MWCNT bio-nanocomposite films	5.86–4.58	25
PVA/PEO	5.9–4.9	26
PMMA/0.15% CB	5–11	26
PVA	4.86	[Present work]
PVA/CB	3.58	[Present work]

[a] The standard deviation is estimated from the Tauc analyses.

using the Wemple–DiDomenico single-oscillator model,[36] which accurately describes the refractive index behavior in the transparent region ($\lambda > 700$ nm). A linear relationship between $(n^2-1)^{-1}$ and E^2, shown in Fig. 4C, confirms the applicability of the model. From the slope and intercept of the fitted line, the dispersion energy ($E_d = 70.3$ eV), oscillator energy ($E_0 = 20.4$ eV), and high-frequency dielectric constant ($\varepsilon_\infty = 1.29$) were extracted. The relatively high E_d value reflects strong interband electronic transitions, indicating an enhanced electronic polarizability that facilitates efficient light–matter interaction. These optical characteristics are directly linked to the photothermal conversion performance of the CB thin film. Strong electronic transitions and high polarizability increase optical absorption, particularly in the visible and near-infrared regions, promoting non-radiative relaxation pathways that convert absorbed photon energy into heat. The moderate oscillator energy further supports broadband absorption, which is advantageous for photothermal applications requiring efficient energy dissipation.

Analysis of the n^2 *versus* λ^2 relationship (eqn (13) and Fig. 4D) yielded a lattice dielectric constant ($\varepsilon_L = 4.48$) and a high carrier concentration-to-effective-mass ratio ($N/m^* = 4.96 \times 10^{50}$ kg^{-1} m^{-3}). The high N/m^* value implies enhanced charge carrier mobility, which facilitates rapid electron–phonon coupling and accelerates thermalization processes. Moreover, the small difference between ε_L (4.48) and ε_∞ (1.29) indicates that electronic polarization dominates the dielectric response, minimizing energy losses associated with ionic polarization and favoring efficient photothermal heat generation. Overall, the strong optical dispersion, high electronic polarizability, and

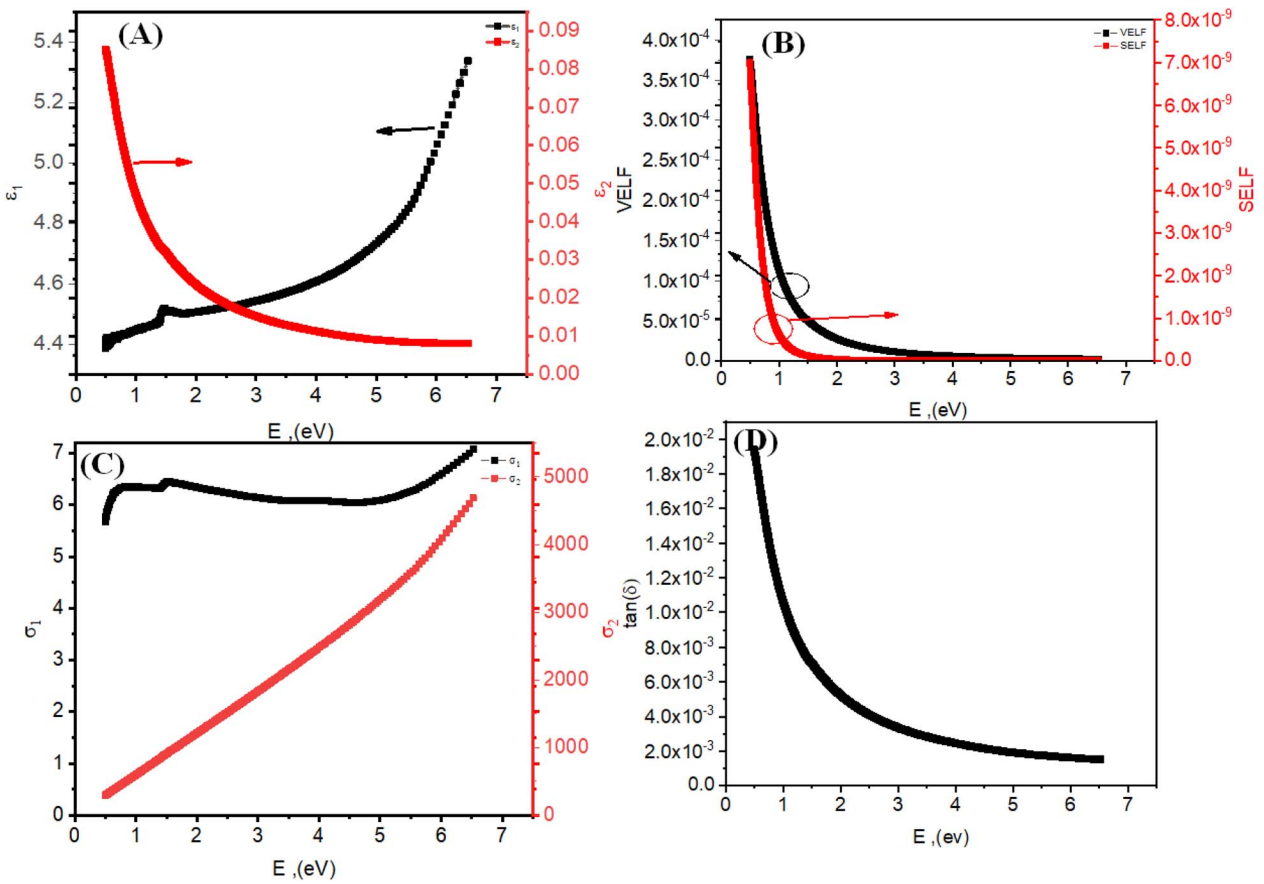

Fig. 5 Plot of the photon energy dependence of real dielectric const. ε_1 (Left side) and imaginary dielectric const. ε_2 (Right side) *versus* E (A). Plot of photon energy dependence of volume energy loss function, VELF (left side), and surface energy loss function, SELF (right side), as a function of E (B). Plot of real optical conductivity, σ_1 (Left side) and imaginary optical conductivity, σ_2 (Right side) *versus* E (C), and plot of nonlinear optical parameter *versus* E (D) of the CB film.

efficient carrier dynamics revealed by the extracted parameters collectively explain the favorable photothermal conversion behavior of the CB thin film, supporting its potential use in photothermal energy harvesting, thermal imaging, and optoelectronic–thermal hybrid devices.

3.2.3. Dielectric characteristics of the CB thin film. Fig. 5A presents the real (ε_1) and imaginary (ε_2) parts of the dielectric function of the CB thin film as a function of photon energy. The gradual increase in $\varepsilon_1(E)$ reflects enhanced polarization and dispersive behavior arising from electronic transitions. The relatively high values of $\varepsilon_2(E)$ at low photon energies indicate strong optical absorption, which is a key prerequisite for efficient photothermal conversion. The decrease in $\varepsilon_2(E)$ with increasing energy suggests that photothermal heat generation is most pronounced in the low-energy (visible-near-IR) region, where photon absorption and subsequent non-radiative relaxation processes dominate.

Fig. 5B presents the Volume Energy Loss Function (VELF) and Surface Energy Loss Function (SELF), offering direct insight into the energy dissipation pathways responsible for photothermal heating. The pronounced low-energy peaks in both functions indicate efficient transfer of incident electromagnetic energy to electronic excitations in the bulk (VELF) and at the surface (SELF). These excitations subsequently relax through non-radiative electron–phonon interactions, converting absorbed optical energy into heat.

The predominance of low-energy loss processes demonstrates that the CB thin film is highly efficient in photothermal energy dissipation, particularly at the surface where localized heating is crucial for photothermal applications. The combined effect of bulk and surface electronic excitations enhances broadband optical absorption and promotes efficient light-to-heat conversion, leading to high photothermal evaporation rates in solar desalination systems. This absorption further localizes heat at the membrane–water interface and minimizes thermal losses to the bulk solution, which is essential for interfacial photothermal applications.[38]

Fig. 5C illustrates the real (σ_1) and imaginary (σ_2) components of the optical conductivity. The increase in $\sigma_1(E)$ at higher photon energies reflects enhanced photo-excited charge carrier transport, which contributes to Joule heating and thus supports photothermal conversion. Meanwhile, the monotonic increase in $\sigma_2(E)$ indicates strong polarization and energy storage effects, which facilitate delayed energy release as heat. Together, these trends demonstrate that optical conductivity plays a central role in converting absorbed photons into thermal energy within the CB thin film.

Fig. 5D displays the loss tangent ($\tan\delta$), a direct indicator of dielectric energy dissipation. The high $\tan\delta$ values at low photon energies confirm substantial dielectric losses, which are directly associated with efficient photothermal heat generation. As photon energy increases, $\tan\delta$ decreases, indicating reduced dissipation and a transition toward more stable dielectric behavior. This trend suggests that the photothermal efficiency of the CB thin film is maximized at lower photon energies, where absorption-driven losses are dominant. The dielectric function, energy loss spectra, optical conductivity, and loss tangent demonstrate that the CB thin film exhibits strong light absorption, efficient energy dissipation, and pronounced non-radiative relaxation processes. These features confirm the CB suitability for photothermal applications.

3.2.4. The nonlinear optical characteristics of the CB film. Fig. 6A shows the calculated first-order $\chi^{(1)}$, third-order $\chi^{(3)}$ optical susceptibilities, and nonlinear refractive index (n_2) of the CB thin film as functions of photon energy, derived from the measured dispersion parameters. The pronounced photon-energy dependence of $\chi^{(3)}$, with elevated values in the visible and near-infrared regions, confirms strong third-order nonlinear optical activity. This behavior arises from electronic transitions governed by the material's band structure and indicates efficient light–matter interaction under high optical fields. Combined with the low dielectric loss (loss tangent, tan δ), these characteristics support the suitability of CB thin films for nonlinear photonic applications requiring high efficiency and minimal energy dissipation.

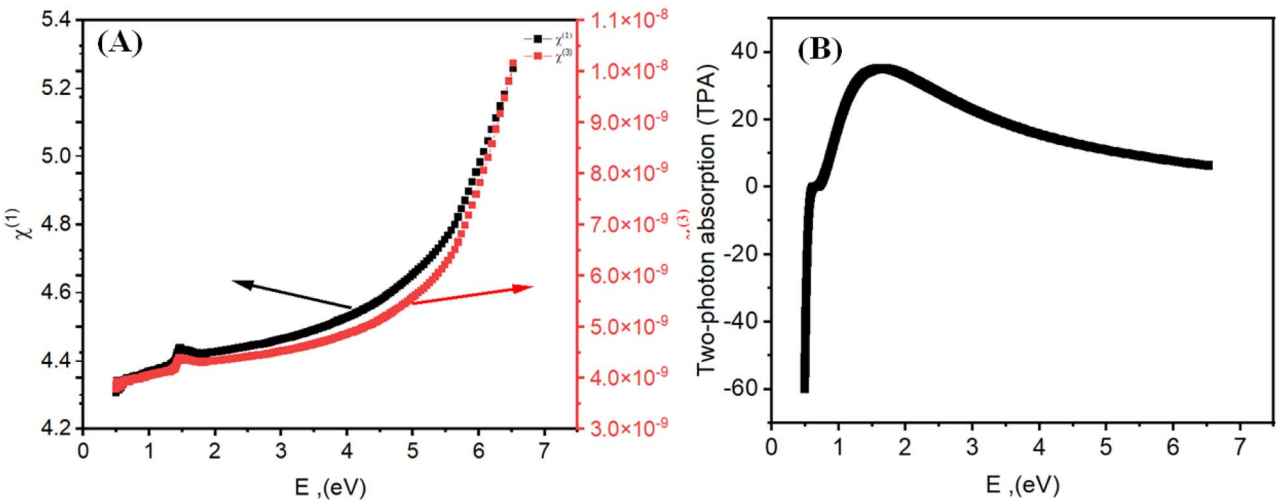

Fig. 6 Plot $\chi^{(1)}$, $\chi^{(3)}$ (A) *n* and TPA (B) *versus E* of CB thin film.

Fig. 6B presents the two-photon absorption (TPA) coefficient as a function of photon energy. At low photon energies (<1 eV), the negative TPA values indicate a saturable absorption regime caused by state filling near the Fermi level. With increasing photon energy, the TPA coefficient becomes positive and reaches a maximum near ~1.5 eV, corresponding to allowed two-photon transitions from π-electron states to higher-energy conduction band states. This strong nonlinear absorption in the visible range enables efficient conversion of optical energy into heat through nonradiative relaxation pathways. At higher energies (>2 eV), the gradual reduction in TPA reflects increased interband absorption and damping effects, signalling a transition toward linear absorption. Overall, the coexistence of high $\chi^{(3)}$, strong visible-range TPA, and low optical losses establishes CB thin films as promising candidates for photothermal conversion, where nonlinear absorption directly enhances localized heat generation under intense optical excitation.

3.3. Characterization of the membranes

The chemical composition and structural integrity of the membranes were evaluated using FTIR spectroscopy. The FTIR spectra confirm successful modification of the PTFE matrix with PVA and CB, Fig. 7. The pristine PTFE spectrum (black) exhibits characteristic bands at 1140 and 1200 cm^{-1}, corresponding to symmetric and asymmetric stretching of CF_2 groups, typical of the PTFE backbone. After PVA incorporation (red spectrum), a broad band at 3200–3500 cm^{-1} appears due to O–H stretching, confirming successful blending. The peak near 2900 cm^{-1} is assigned to aliphatic C–H stretching, while bands at 1420–1320 cm^{-1} correspond to C–H and O–H bending vibrations. The region between 1080 and 1140 cm^{-1} is attributed to C–O stretching of secondary alcohol groups, and bands at 840–920 cm^{-1} are associated with polymer backbone vibrations.[27–29] In the PVA–CB composite (blue spectrum), slight shifts and intensity changes in the O–H band indicate hydrogen

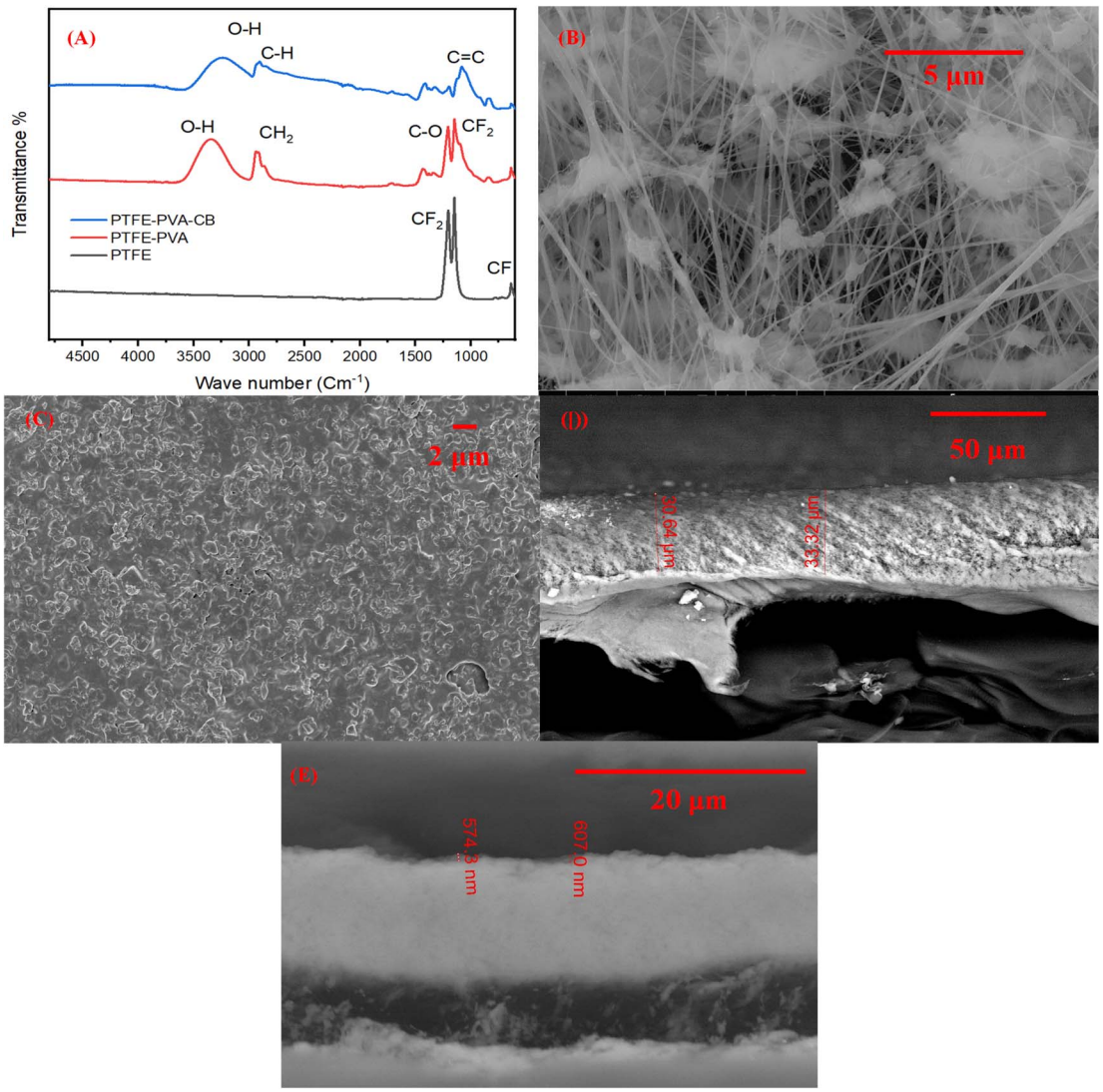

Fig. 7 (A) FTIR spectra of PTFE, PTFE–PVA, and PTFE–PVA–CB membranes (B) SEM image of pristine PTFE surface. (C) SEM image of modified PTFE/PVA–CB membrane surface. (D) Cross-sectional SEM image of pristine PTFE. (E) Cross-sectional SEM image of modified membrane, showing the formation of a uniform photothermal layer.

bonding and interfacial interactions between PVA and CB. The characteristic C–F stretching of PTFE remains evident as a strong doublet at ~1204 and 1150 cm^{-1}, with an additional band near 636 cm^{-1} corresponding to CF_2 bending vibrations. These results confirm successful integration of all components without disrupting the PTFE structure.[30] SEM images (Fig. 7B and C) show that the pristine PTFE membrane possesses a typical expanded fibrous network with interconnected fibrils and nodes, forming a highly porous structure. This morphology provides high surface area, strong hydrophobicity, and a pore size consistent with the nominal 0.45 μm rating, supporting high vapor permeability and stable liquid entry pressure in membrane distillation. After coating, the PTFE/PVA–CB membrane exhibits a uniform and continuous photothermal layer. The surface becomes smoother while retaining slight micro-roughness, indicating that the coating is thin and does not block pores. This confirms effective deposition and strong adhesion between the coating and the substrate, which is essential for maintaining hydrophobicity and preventing pore wetting.[30,31]

Cross-sectional SEM analysis (Fig. 7D and E) shows an overall membrane thickness of approximately 30–33 μm and a well-defined active layer with a thickness of 574–607 nm. This thin, uniform layer reflects good control over the coating process and minimizes additional mass transfer resistance.[6] The image confirms a robust, cohesive structure, indicating good mechanical stability for the composite membrane. The photothermal layer plays a critical role by enabling solar absorption through CB while preserving the membrane's porous structure. Its minimal thickness and uniformity ensure that vapor transport is not hindered. Functionally, this structure enhances membrane distillation performance by promoting localized heating at the membrane–feed interface, reducing temperature polarization, and increasing vapor flux. At the same time, the underlying PTFE structure maintains hydrophobicity and mechanical stability, addressing common limitations of conventional membranes such as low thermal efficiency and wetting. At higher loadings, CB nanoparticles may aggregate due to strong van der Waals interactions, leading to non-uniform coatings and reduced performance. In this study, CB content was optimized to ensure uniform dispersion, as supported by SEM observations. Further improvements could be achieved through nanoparticle functionalization, dispersing agents, or ultrasonication, which would enhance stability, coating uniformity, and long-term performance.

3.3.1. Mechanism of dual-layer membrane assembly: interlocking and covalent cross-linking. The formation of the stable bilayer photothermal membrane and its interaction with the chemically inert PTFE substrate are illustrated in Fig. 8. The adhesion mechanism combines physical interlocking with selective chemical cross-linking within the PVA layer, without forming covalent bonds with the PTFE support. As shown in Fig. 8A, adhesion of the hydrophilic PVA–CB photothermal layer to the hydrophobic PTFE substrate ($[-CF_2-CF_2-]_n$) is primarily governed by mechanical interlocking. The process begins with ethanol pre-wetting of the PTFE membrane,[32] which temporarily lowers its surface energy and enables effective wetting by the aqueous PVA–CB suspension.

The PVA–CB suspension (PVA matrix in blue with dispersed CB nanoparticles) is then spray-coated onto the membrane. The reduced surface energy, combined with spray atomization, allows partial infiltration of PVA chains into the microporous PTFE structure. Upon drying, water evaporation induces chain entanglement, physically trapping the PVA within the fibrous, nodular pore morphology. This results in strong and durable anchoring of the photothermal layer without the need for chemical bonding. Fig. 8B illustrates the acid-catalyzed cross-linking of the PVA matrix using glutaraldehyde (GA), which occurs exclusively within the PVA layer and does not alter the PTFE substrate. Under acidic conditions, GA functions as

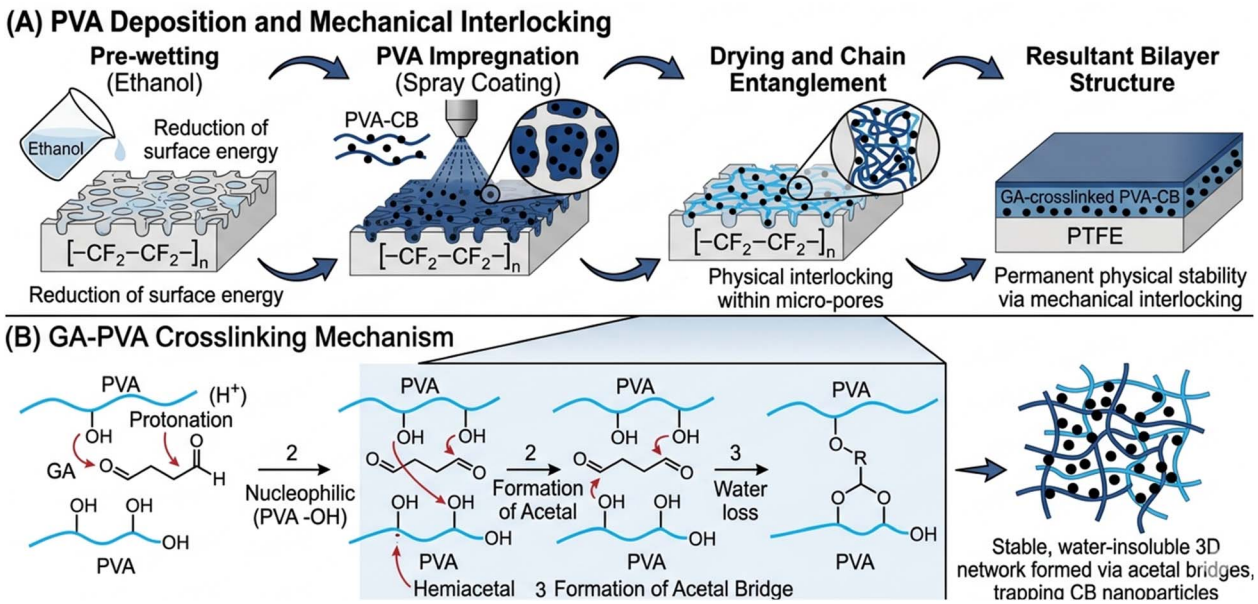

Fig. 8 Schematic illustration of the membrane fabrication process (A), and the dual-mechanism for layer stabilization (B).

a bifunctional cross-linker *via* its two aldehyde (–CHO) groups.[33,34] Each GA molecule reacts with two hydroxyl (–OH) groups from adjacent PVA chains, forming stable acetal bridges. The mechanism involves nucleophilic attack of a PVA –OH group on a protonated aldehyde, generating a hemiacetal intermediate, followed by a second nucleophilic attack that releases water and forms a robust acetal linkage (–O–CH–$(CH_2)_3$–CH–O–).[32,35] The repeated formation of these acetal bridges transforms linear, water-soluble PVA into a dense, insoluble three-dimensional network. This cross-linked structure immobilizes the CB nanoparticles and significantly enhances the mechanical stability and durability of the photothermal layer.[32]

3.4. Membrane distillation applications

3.4.1. Surface wettability and liquid entry pressure. The surface wettability of the membranes was assessed by measuring the static water contact angle (θ) using the sessile drop method with deionized water (DI-water) as the probe liquid. Measurements were performed at room temperature using a contact angle goniometer, with at least five measurements per sample to ensure reproducibility as shown in Fig. 9A. The pristine PTFE membrane exhibited a contact angle of 105.5° ± 2.5°, confirming its inherent hydrophobicity, which is essential for preventing liquid penetration into the pores during MD operation. Incorporation of PVA alone significantly reduced the contact angle to 58.7° ± 2.6°, reflecting the hydrophilic nature of PVA due to its abundant hydroxyl groups. The addition of CB to the PVA matrix partially restored hydrophobicity, with contact angles increasing to 71.7° ± 2.8° for 0.75 wt% CB and 75.6° ± 4.6° for 1 wt% CB. This improvement can be attributed to the hydrophobic nature of CB nanoparticles and their uniform dispersion within the PVA matrix, which reduces the overall surface energy of the composite coating.

3.4.2. Wetting resistance and liquid entry pressure (LEP) estimation. The Liquid Entry Pressure (LEP) is a critical parameter for evaluating the anti-wetting capability of membranes in Membrane Distillation (MD) applications. It defines the minimum hydrostatic pressure required for the feed solution to penetrate the membrane pores. For the pristine PTFE membrane (θ = 105.5°), the estimated liquid entry pressure (LEP) is ~0.8 bar, consistent with reported values for similar commercial PTFE membranes (typically 1–4 bar, depending on pore size and test conditions). Although the coated membranes exhibit lower contact angles due to the hydrophilic PVA layer on the feed-facing side, the coating strategy—controlled low-concentration spray deposition, mild ethanol pre-wetting to enhance adhesion without deep penetration, and glutaraldehyde crosslinking—ensures that the PVA–CB layer remains a thin surface film. As a result, it does not significantly infiltrate or alter the hydrophobic internal pore structure of the PTFE substrate.[36,37] This creates a Janus configuration: a hydrophilic feed surface that enhances water transport and photothermal performance, while the internal pores and permeate side remain hydrophobic. Consequently, the membrane preserves its LEP and resists liquid breakthrough. The sustained salt rejection (>99%) during MD operation further confirms the absence of pore wetting. The measured LEP (~0.76 bar) falls within the expected range for PTFE membranes with similar pore sizes and remains well above typical MD operating pressures, ensuring stable, wetting-resistant performance.

Fig. 9B illustrates the liquid entry pressure (LEP) values of the pristine PTFE membrane and the modified PVA/CB

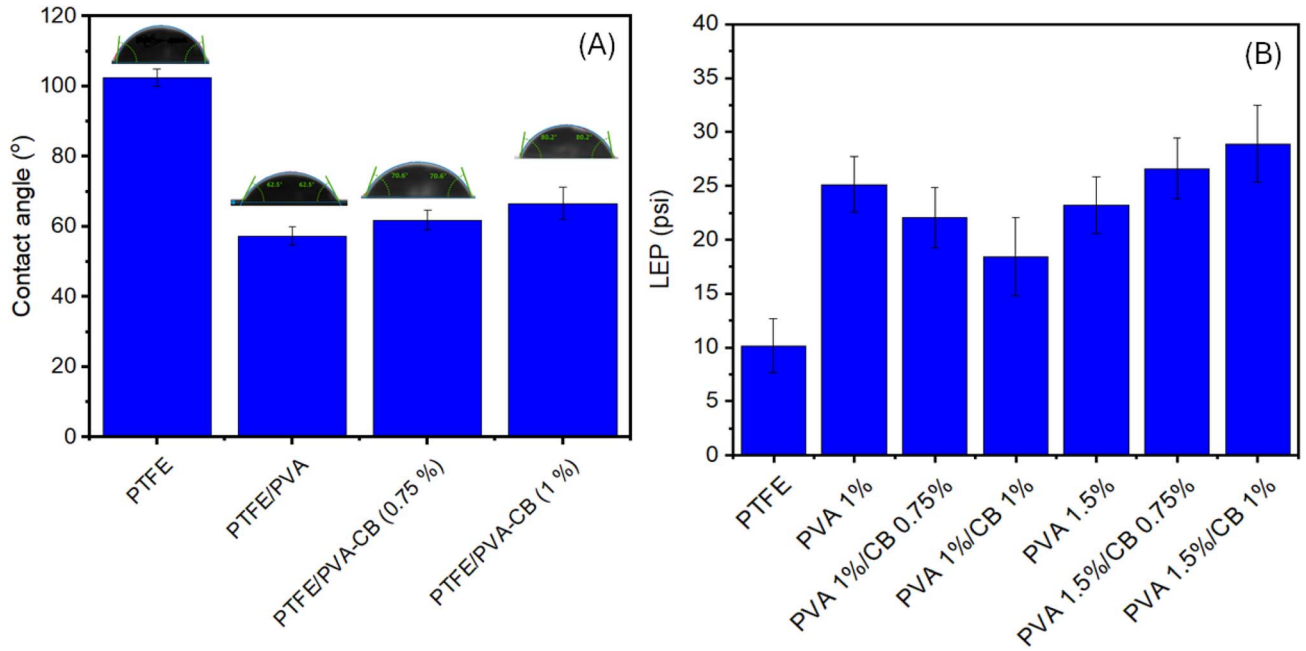

Fig. 9 (A) Water contact angle measurements of PTFE, PTFE/PVA, PTFE/PVA–CB (0.75%), and PTFE/PVA–CB (1%) membranes, (B) liquid entry pressure (LEP) values of the pristine PTFE membrane and the modified PVA/CB composite membranes.

composite membranes. The pristine PTFE membrane exhibited the lowest LEP value (~10.1 psi), which can be attributed to its relatively larger effective pore size and the absence of a surface-modifying layer. Upon incorporation of polyvinyl alcohol (PVA) and carbon black (CB), a significant increase in LEP was observed. Notably, the PTFE/PVA (1.5%)/CB (1%) membrane achieved the highest LEP value (~29.2 psi), corresponding to an enhancement of approximately 190% compared to the pristine membrane.[38] This improvement can be explained based on the Young–Laplace equation,

$$\mathrm{LEP} = \frac{-2\gamma B \cos\theta}{r_{\max}} \tag{18}$$

where LEP is inversely proportional to the maximum pore radius and directly influenced by surface properties. The enhancement is primarily attributed to two synergistic effects; reduction in effective pore size due to partial pore coverage and filling by the PVA/CB coating layer, leading to a decrease in $r_{\max}$, and improved structural integrity and surface uniformity provided by the PVA matrix reinforced with CB nanoparticles, which enhances resistance to liquid penetration. A slight fluctuation in LEP at lower PVA concentration (1%) with increasing CB content may be associated with nanoparticle agglomeration, causing local heterogeneity in pore distribution. In contrast, at higher PVA concentration (1.5%), the membrane exhibits improved stability and more uniform coverage, resulting in superior wetting resistance. Overall, the PTFE/PVA (1.5%)/CB (1%) membrane demonstrates excellent resistance to pore wetting, making it a promising candidate for long-term membrane distillation applications without compromising permeate quality.[32,39,40]

3.4.3. Surface temperature and polarization of the membranes. In this study, a tungsten lamp with an intensity of 30 W m^{-2} was used as the light source. Fig. 10A shows the temporal evolution of membrane surface temperature under illumination and after the light is switched off at lamp–membrane distances of 10, 15, and 20 cm. According to the inverse square law, light intensity decreases rapidly with increasing distance. Upon illumination, the surface temperature rises rapidly at all distances, indicating efficient photothermal conversion and fast heat accumulation. At 10 cm, the membrane reaches the highest steady-state temperature (~58 °C), consistent with the higher light intensity at shorter distances. The temperature then stabilizes, suggesting thermal equilibrium between heat generation and dissipation. After the light is turned off, the temperature drops sharply, followed by gradual cooling toward ambient conditions. At 15 cm, a similar trend is observed, with a slightly lower maximum temperature (~57 °C) and a slower approach to steady state due to reduced light intensity. The cooling behavior remains comparable, although the stored thermal energy is lower. At 20 cm, both the heating rate and maximum temperature (~50–51 °C) decrease significantly, confirming the strong dependence of photothermal performance on distance. Cooling is again rapid, reflecting limited heat retention. Generally, Fig. 10A demonstrates that reducing the distance between the light source and the membrane enhances photothermal heating, resulting in higher temperatures and faster heating rates. This effect is important for optimizing light-driven membrane systems, where light–membrane geometry directly influences thermal performance and efficiency.

Temperature polarization (TP) is a major limitation in conventional MD, causing the membrane surface temperature on the feed side (T_{fm}) to be significantly lower than the bulk feed temperature (T_{fb}), reducing the vapor pressure driving force. The Temperature Polarization Coefficient (TPC) quantifies this effect as.[41,42]

$$\mathrm{TPC} = \frac{T_{\mathrm{fm}} - T_{\mathrm{pm}}}{T_{\mathrm{fb}} - T_{\mathrm{pb}}} \tag{19}$$

where T_{pm} and T_{pb} are the permeate-side membrane surface and bulk temperatures, respectively.

In this study, membrane surface temperatures were measured under simulated solar irradiation (Fig. 10A) to evaluate interfacial thermal conditions. The pristine PTFE membrane exhibited pronounced temperature polarization (TP)

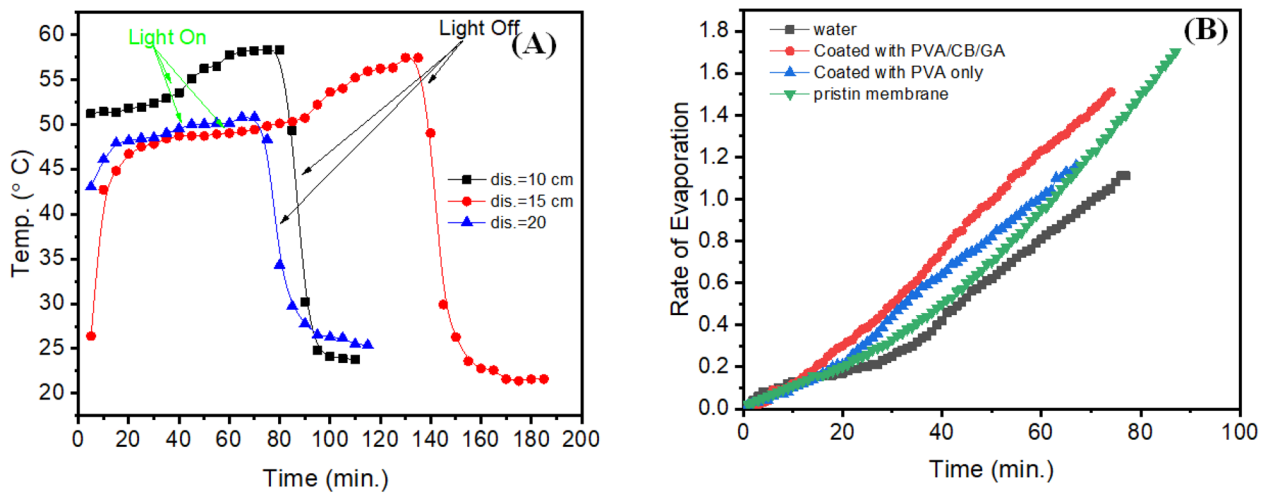

Fig. 10 Effect of the light source distance on membrane surface temperature (A), evaporation rate under simulated solar irradiation (B).

due to limited convective heat transfer. In contrast, the PVA–CB coated membrane showed rapid surface heating, reaching ~58 °C at a 10 cm lamp distance, and maintained a stable temperature significantly higher than the bulk feed under localized photothermal conditions.[36]

Assuming typical bulk temperatures ($T_{fb} = 70$ °C, $T_{pb} = 20$ °C) and estimating the membrane surface temperature ($T_{fm} \approx 58$ °C, with $T_{pm} \approx T_{pb}$ due to effective cooling), the temperature polarization coefficient (TPC) for the modified membrane is approximately 0.76–0.95, depending on interfacial conditions.[43,44] This represents a clear improvement over conventional membrane distillation systems, where TPC values typically range from 0.5 to 0.7 in the absence of localized heating.[41]

The enhanced performance is attributed to the photothermal effect of the CB coating, which localizes heat at the feed–membrane interface, reduces thermal boundary layer resistance, and can even reverse TP under strong illumination (TPC > 1 if $T_{fm} > T_{fb}$). This is consistent with the observed flux enhancement (45–60%) and stable operation, as reduced TP increases the effective vapor pressure gradient and mass transfer efficiency. Comparable studies using carbon-based photothermal materials report TPC values of 0.8–1.2 under irradiation supporting the effectiveness of localized heating in mitigating temperature polarization.[43,44]

3.4.4. Rate of evaporation measurement under simulated solar irradiation. Fig. 10B presents the evolution of evaporation rate over time for pure water and the tested membranes: pristine PTFE, PTFE/PVA, and PTFE/PVA–CB. For all cases, the evaporation rate increases nearly linearly with time, indicating a stable and continuous process under illumination. Pure water shows the lowest evaporation rate, as expected due to the absence of photothermal enhancement. The pristine PTFE membrane exhibits a significantly higher rate, demonstrating the role of its structure in promoting interfacial evaporation through effective heat localization at the water–air interface, reaching approximately 1.3–1.4 L m^{-2} h^{-1} by the end of the experiment. The PTFE/PVA membrane shows a reduced evaporation rate compared to pristine PTFE, although it remains higher than pure water. This behavior is attributed to the hydrophilicity of PVA, which enhances water transport but also increases heat dissipation into the bulk, lowering interfacial heating efficiency. In contrast, the PTFE/PVA–CB membrane exhibits a clear improvement over PTFE/PVA, particularly at longer times, as reflected by the steeper slope of its evaporation curve. This enhancement arises from the incorporation of CB, which acts as an efficient photothermal absorber, improving light absorption and heat localization. The combined effects of PVA and CB enhance vapor transport and thermal management.

3.4.5. Evaluation of MD performance. Fig. 11A illustrates the combined effect of PVA incorporation and CB addition on the water flux as a function of the concentration ratio (C/C_0, where C_0 is the initial salt concentration). The pristine membrane exhibited the lowest flux across the entire range, whereas all modified membranes showed a significant enhancement in water permeation. In the case of PVA modification, the improvement became more pronounced with increasing PVA content, where the membrane containing 1.5 wt% PVA maintained a higher and more stable flux even at elevated C/C_0 values. This enhancement is attributed to the increased hydrophilicity and the formation of interconnected hydrophilic transport pathways induced by the hydroxyl groups of PVA, which facilitate water diffusion across the membrane matrix. On the other hand, the influence of CB loading on water flux under similar operating conditions. The incorporation of CB (0.5–1 wt%) into the PVA-coated membranes further improved water flux compared with the pristine sample, with

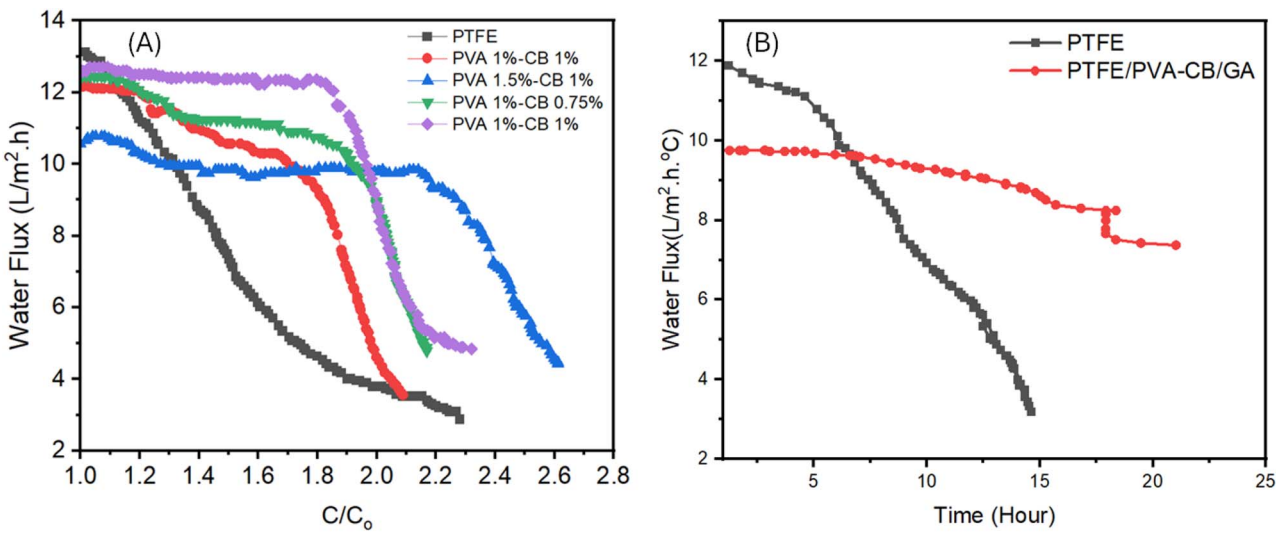

Fig. 11 (A) Comparative analysis of long-term water flux stability as a function of concentration factor (C/C_0) for pristine and modified membranes. (B) Long-term stability of water flux as a function of time for pristine PTFE and PTFE/PVA–CB membranes under MD operation. Operation conditions: feed was 1 L of synthetic brine, the feed and distillate sides flow rates were 0.8 and 0.4 L min^{-1}, respectively, with feed and permeate temperatures of 70 °C, and 20 °C, respectively.

the 1.0 wt% CB membrane achieving the highest performance. This improvement is mainly ascribed to the superior broadband light absorption and photothermal conversion capability of CB, which generates localized heating at the membrane interface, thereby reducing temperature polarization and enhancing the vapor pressure driving force. In conclusion, the incorporation of both PVA and CB significantly enhances water transport properties through a synergistic mechanism that combines improved hydrophilicity and efficient photothermal heat generation. The optimized structure, particularly at 1.5 wt% PVA and 1 wt% CB, provides a thin, porous, and thermally active layer that promotes efficient vapor transport, making the modified membranes highly promising candidates for advanced photothermal membrane distillation applications.

However, a clear trade-off exists between light absorption efficiency and mass transfer resistance. Higher CB loading improves solar-to-heat conversion (due to increased absorber density and reduced reflectance), leading to greater flux enhancement under illumination. Conversely, excessive CB or thicker coatings can increase mass transfer resistance by partially reducing porosity or increasing tortuosity in the coating layer, thereby limiting vapor transport in the absence of strong photothermal driving force. In our experiments, the thin nature of the spray-deposited coating (controlled by low solution concentration, sonication for uniform dispersion, and crosslinking with glutaraldehyde) minimized this resistance, preserving high vapor permeability while enabling effective photothermal localization. Similar trade-offs have been reported in related photothermal MD systems using CB or carbon-based absorbers on PTFE substrates.[2,30,45] For instance, optimal CB concentrations around 0.75–1 wt% in PVA matrices, combined with pore formers (*e.g.*, $LiNO_3$), balanced absorption and porosity and yielded flux enhancements of 45–70% under solar simulation without significant permeability loss. In our case, the 1 wt% CB composition represents an effective optimum, providing substantial photothermal flux gain (up to 45–60% relative to pristine PTFE) while maintaining >99% salt rejection and operational stability, as excessive concentrations could introduce unnecessary resistance or agglomeration issues. These findings underscore the importance of systematic optimization in photothermal coating design, where thin, porous layers maximize the benefits of localized heating while minimizing additional transport barriers.

To evaluate the separation efficiency of the PVA–CB modified membrane, the salt rejection (R%) was monitored throughout the MD process. The modified membrane demonstrated a remarkably high salt rejection exceeding 99.9%. This indicates that the thin PVA–CB photothermal layer did not compromise the membrane's hydrophobicity or induce pore wetting; rather, it effectively enhanced the vapor flux while maintaining excellent salt separation integrity.

To evaluate the long-term operational stability of the membranes, the water flux was monitored as a function of time over an extended period, as shown in Fig. 11B. The pristine PTFE membrane exhibited a significant and continuous decline in flux, which can be attributed to temperature polarization and possible fouling or scaling effects during operation. In contrast, the PVA–CB/PTFE membrane demonstrated a much more stable flux with only a gradual decrease over time. This enhanced stability can be attributed to the synergistic effects of improved hydrophilicity from PVA and localized photothermal heating from CB, which together mitigate temperature polarization and reduce the accumulation of foulants on the membrane surface. These results confirm that the modified membrane exhibits superior long-term stability and resistance to performance degradation compared to the pristine membrane. The reduced flux decline suggests suppressed fouling/scaling tendencies, which can be attributed to improved interfacial heat localization and reduced bulk heat dissipation. The performance of the photothermal membrane is strongly influenced by the spray-coating parameters, particularly the thickness and uniformity of the deposited layer. A uniform and well-controlled coating ensures homogeneous light absorption and efficient photothermal heat generation across the membrane surface. However, excessive coating thickness may increase mass transfer resistance by partially blocking membrane pores or increasing vapor diffusion path length, leading to reduced flux. Conversely, insufficient coating thickness may result in poor light absorption and weak photothermal conversion. In this study, the spray-coating conditions were carefully adjusted to achieve a uniform and optimized coating layer, as confirmed by SEM observations. The resulting membrane exhibits a balanced performance, combining efficient photothermal heating with minimal mass transfer resistance, leading to enhanced flux and stable operation. This trade-off between optical absorption and mass transfer resistance highlights the importance of coating optimization in photothermal MD systems.

3.4.6. Photothermal feed-to-vapor efficiency. To provide a quantitative assessment of the energy efficiency of the photothermal process, the solar-to-vapor (or photothermal feed-to-vapor) efficiency (η) was calculated using the standard formula for interfacial photothermal systems:

$$\eta = \frac{Jh_{fg}}{I} \times 100\% \quad (20)$$

where J is the vapor flux (L m^{-2} h^{-1}), h_{fg} is the latent heat of vaporization of water ($\approx$2400 kJ kg^{-1} at operating temperatures of 40–70 °C), and I is the incident solar irradiance (W m^{-2}).

Under simulated solar irradiation (assuming 1 sun equivalent, I = 1000 W m^{-2}, based on typical conditions for the reported flux enhancement), the PVA–CB modified membrane achieved a vapor flux of up to 1.3 L m^{-2} h^{-1}, corresponding to a photothermal efficiency of approximately 87%. This value reflects the efficient conversion of incident solar energy into localized heat at the membrane surface, driving vapor generation with minimal thermal losses to the bulk feed due to the photothermal localization effect of the CB coating. This efficiency is competitive with or superior to recent photothermal MD systems using carbon-based absorbers (*e.g.*, 70–85% in CB/PVA or graphene composites under 1 sun), highlighting the advantage of the thin, spray-deposited turbostratic CB layer in broadband absorption and heat localization. The high η supports the claim of energy-efficient performance, as it

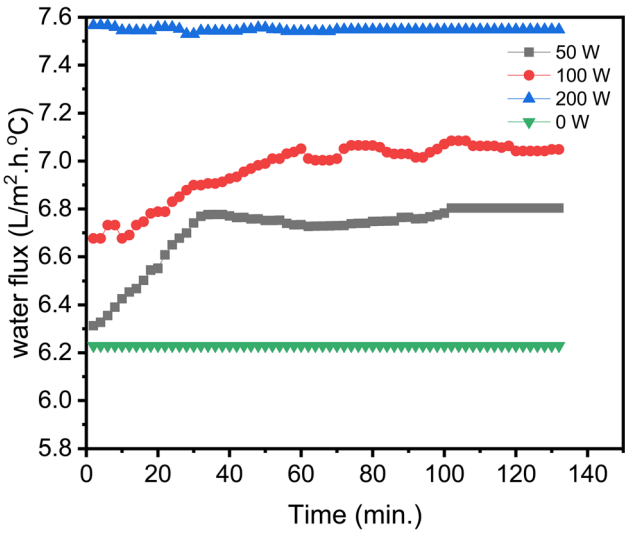

Fig. 12 Time-dependent water vapor flux under simulated solar irradiation for the PVA (1.5 wt%)/CB (1 wt%) coated membrane at 50, 100, 200 W m^{-2}.

significantly reduces the specific thermal energy consumption compared to conventional MD (where external heating dominates). Further optimization of irradiance levels (as shown in Fig. 12 at (50–200 W m^{-2}) and long-term stability could push efficiencies toward 90%, aligning with state-of-the-art interfacial photothermal distillation.[46,47] Fig. 12 presents the temporal photothermal response of pristine and modified membranes under simulated solar irradiation. The PVA–CB coated PTFE membrane exhibits a rapid temperature rise followed by a stable plateau at a significantly higher level than the pristine PTFE membrane, confirming its superior photothermal conversion capability. In contrast, the pristine PTFE shows only a moderate temperature increase, while the uncoated control sample displays negligible thermal response, indicating minimal light-to-heat conversion.

The markedly enhanced heating of the PVA–CB membrane is directly attributed to the strong broadband optical absorption of CB and the improved interfacial wettability induced by PVA, which together promote efficient heat localization at the membrane surface. This enhanced photothermal effect correlates well with the optical characterization results, including the reduced reflectance and narrowed optical band gap, and explains the observed increase in vapor flux and reduced temperature polarization during membrane distillation operation. The stable temperature profile over time further indicates the good photothermal stability and durability of the composite coating under prolonged irradiation.

Table 2 presents a comparative analysis of photothermal efficiency for various membrane systems employed in solar-driven or photothermal membrane distillation (PMD). The PVA–CB/PTFE membrane developed in this study demonstrates a vapor flux of 1.3 L m^{-2} h^{-1} under 1 sun irradiation, achieving a photothermal efficiency (η) of approximately 87%. This performance is competitive with other CB-based systems (70–85%) and graphene/PVA-based membranes (~70%), while maintaining a relatively low fabrication cost.[30] Notably, the PVDF/g-C_3N_4 nanosheet-embedded membrane exhibits a significantly higher vapor flux of 27.63 L m^{-2} h^{-1} under 1 sun irradiation with a photothermal efficiency of 70%. However, this high flux is typically obtained in conventional direct contact membrane distillation (DCMD) configurations assisted by localized heating rather than pure passive solar-driven systems. In contrast, the PPy@PVA-PVDF/F-SiO_2-PVDF Janus membrane and the MXene-PVA-TiO_2@PVDF photothermal-catalytic membrane show lower fluxes (4.17 L m^{-2} h^{-1} and 1.23 L m^{-2} h^{-1}, respectively) but offer additional advantages in fouling resistance and oil-contaminated feed treatment.[51] The table highlights the superiority of the PVA–CB/PTFE membrane developed in this study, achieving high efficiency (≈87%) compared to other low-cost systems (such as CB-based PMD and Graphene/PVA PMD), while maintaining competitive vapor flow under 1 sun without the need for irradiation intensification. It also surpasses high-cost systems in terms of economic viability, although some (such as photothermal MD) achieve higher efficiency (95%) or higher flux under intense irradiation conditions (PP@PVA).

3.5. Economic and environmental considerations

The economic viability of the proposed membrane is rooted in its reliance on low-cost, earth-abundant materials. By utilizing CB as an efficient photothermal absorber and PVA as a hydrophilic matrix, the material costs are significantly minimized compared to high-end alternatives like graphene or MXenes. Furthermore, the fabrication employs a scalable spray-coating technique, which avoids complex, energy-intensive synthesis routes. This approach achieves a high solar-to-vapor conversion efficiency of approximately 87% under 1 sun while maintaining robust anti-scaling properties, making it a cost-effective solution for large-scale, off-grid desalination. From a sustainability perspective, the solar-driven nature of this MD process drastically reduces dependency on fossil fuels, leading to a substantial decrease in greenhouse gas emissions. The localized

Table 2 Photothermal efficiency comparison

Membrane/system	Irradiance (W m^{-2})	Vapor flux (L m^{-2} h^{-1})	Efficiency η (%)	Cost	Reference
PVA–CB/PTFE	1000 (1 sun)	1.3	~87	Low	This study
CB-based PMD	1000 (1 sun)	~1.0–1.5	70–85	Low	2 and 45
Graphene/PVA PMD	1000 (1 sun)	~1.2	~70	High	48
Photothermal MD	1000 (1 sun)	2.17	95	High	3
PPy@PVA-PVDF/F-SiO_2-PVDF	under 3 sun intensity	4.17	77.33	Low	49
MXene-PVA-TiO_2@PVDF (photothermal-catalytic membrane)	1 sun irradiation	1.23	—	Low	50

photothermal heating at the membrane–water interface enhances energy utilization by mitigating temperature polarization and reducing bulk heat losses. Life-cycle assessment (LCA) data suggests that this configuration can reduce environmental burdens, including human health impacts and resource depletion by up to 80% compared to conventional thermal MD systems. Additionally, the PVA–CB coating improves membrane durability, extending its operational lifespan and reducing material waste. The synergy between cost-efficiency and environmental performance positions this technology as a sustainable solution for regions facing acute water scarcity. By minimizing both CAPEX and OPEX, the system is uniquely suited for decentralized applications in remote areas with limited access to traditional energy grids.

4. Conclusion

This study introduces a new perspective by integrating optical physics with membrane distillation performance, providing a fundamental framework for the rational design of photothermal membranes. The aim was to enhance membrane performance through the combined effects of improved surface wettability and photothermal heating. Structural characterization showed that the CB particles possess a turbostratic graphitic structure with a crystallite size of 36.3 nm and a microstrain of 3.44×10^{-4}. Optical analysis revealed a direct band gap of 3.58 eV, indicating strong light absorption and promising photothermal properties. Incorporating CB and PVA into the PTFE membrane significantly improved MD performance compared with pristine membranes. The addition of PVA increased membrane hydrophilicity and facilitated water transport, while CB enhanced thermal conductivity and photothermal conversion, promoting more efficient vapor generation. Among the tested compositions, the membranes containing 1.5 wt% PVA and 1 wt% CB exhibited the highest and most stable water flux across all feed concentrations. The improved performance is attributed to the synergistic interaction between enhanced surface wettability and localized photothermal heating, which together promote efficient heat and mass transfer during MD operation. These findings demonstrate that PVA–CB composite coatings offer a simple, scalable, and cost-effective strategy for developing durable, high-performance membranes for photothermal desalination and advanced water treatment. The developed PVA–CB/PTFE membrane demonstrated a significant enhancement in membrane distillation performance, achieving a maximum vapor flux of approximately 1.3 L m^{-2} h^{-1}, representing an improvement of about 45–60% compared to the pristine PTFE membrane. This enhancement is attributed to the synergistic effects of improved hydrophilicity and efficient photothermal conversion, which reduce temperature polarization and enhance vapor transport. In addition, the membrane maintained excellent salt rejection (>99%) and stable operation over extended periods, confirming its resistance to pore wetting and performance degradation. These results highlight the effectiveness of the proposed design in simultaneously improving flux, efficiency, and operational stability.

Conflicts of interest

There are no conflicts to declare.

Data availability

The data that support the findings of this study are available from the corresponding author upon reasonable request.

Supplementary information (SI) is available. See DOI: https://doi.org/10.1039/d6ra02032a.

Acknowledgements

We would like to extend my sincere gratitude to the dedicated team at the Water Technologies Innovation Institute and Research Advancement (WTIIRA) in Jubail, Saudi Arabia, for their outstanding efforts and support in accomplishing this project.

References

1 M. Pyo, *et al.*, A study on the measurement conditions for determining liquid entry pressure values of hydrophobic membranes, *Chem. Eng. Res. Des.*, 2024, **208**, 184–193.
2 M. E. Ali, *et al.*, Spray-coated porous photothermal layer on PTFE membranes for robust anti-scaling and solar membrane distillation, *Desalination*, 2024, **573**, 117196.
3 M. Talebi, *et al.*, Development of Janus PSF/PVA Membranes for Efficient Desalination *via* Membrane Distillation, *Polym. Eng. Sci.*, 2026, **66**(1), 204–212.
4 T. Altalhi, *et al.*, Optical spectroscopic studies on poly (methyl methacrylate) doped by charge transfer complex, *Opt. Mater.*, 2021, **117**, 111152.
5 M. El-Nahass, *et al.*, Effect of illumination on the structural and optical properties of Cu (II) tetraphenyl porphyrin (CuTPP) thin films, *Opt. Commun.*, 2014, **325**, 116–121.
6 M. S. Hossain and S. Ahmed, Easy and green synthesis of TiO2 (Anatase and Rutile): Estimation of crystallite size using Scherrer equation, Williamson-Hall plot, Monshi-Scherrer Model, size-strain plot, Halder-Wagner Model, *Results Mater.*, 2023, **20**, 100492.
7 R. Peymanfar, E. Selseleh-Zakerin and A. Ahmadi, Tailoring energy band gap and microwave absorbing features of graphite-like carbon nitride (g-C3N4), *J. Alloys Compd.*, 2021, **867**, 159039.
8 S. Wemple and M. DiDomenico Jr, Optical dispersion and the structure of solids, *Phys. Rev. Lett.*, 1969, **23**(20), 1156.
9 B. Ebraheem, *et al.*, Enhancement of optical absorption and dispersion characteristics of nanocrystalline In2Se3 films: impact of γ-ray irradiation, *J. Mater. Sci.: Mater. Electron.*, 2023, **34**(5), 382.
10 B. Ebraheem, *et al.*, Nanocrystalline embedded In_2Se_3 amorphous thin film investigation and optical enhancement characterization for photo-sensing application, *Indian J. Phys.*, 2023, **97**(3), 885–896.
11 C. A. Love-Baker, *et al.*, Analysis of the turbostratic structures in PAN-based carbon fibers with wide-angle x-ray diffraction, *Carbon*, 2024, **224**, 119037.

12 P. Kibasomba, *et al.*, Strain and grain size of TiO_2 nanoparticles from TEM, Raman spectroscopy and XRD: the revisiting of the Williamson-Hall plot method, *Results Phys.*, 2018, **9**, 628–635.
13 I. G. Shitu, *et al.*, X-ray diffraction (XRD) profile analysis and optical properties of Klockmannite copper selenide nanoparticles synthesized *via* microwave assisted technique, *Ceram. Int.*, 2023, **49**(8), 12309–12326.
14 P. M. Kibasomba, *et al.*, Strain and grain size of TiO2 nanoparticles from TEM, Raman spectroscopy and XRD: The revisiting of the Williamson-Hall plot method, *Results Phys.*, 2018, **9**, 628–635.
15 N. T. Tayade and M. P. Tirpude, Frustrated microstructures composite PbS material's size perspective from XRD by variant models of Williamson–Hall plot method, *Bull. Mater. Sci.*, 2023, **46**, 20.
16 C. Regmi, Y. K. Kshetri and S. R. Wickramasinghe, Carbon-based nanocomposite membranes for membrane distillation: progress, problems and future prospects, *Membranes*, 2024, **14**(7), 160.
17 H. Zeyada, *et al.*, Spectral, structural, optical and dielectrical studies of UV irradiated Rose Bengal thin films prepared by spin coating technique, *Phys. B*, 2017, **506**, 75–82.
18 N. Assoudi, *et al.*, Unconventional critical behavior near the phase transition temperature and magnetocaloric effect in La0. 5Ca0. 4Ag0. 1MnO3 compound, *Chem. Phys. Lett.*, 2018, **706**, 182–188.
19 R. A. Shehzad, *et al.*, Enhanced linear and nonlinear optical response of superhalogen (Al7) doped graphitic carbon nitride (g-C3N4), *Optik*, 2021, **226**, 165923.
20 I. Al-Mosawi Ali, H. Al-Maamori Mohammad and H. Al-Mayalee Khalidah, Spectroscopic studies of polyester-carbon black composites, *Res. J. Mater. Sci.*, 2013, **2320**, 6055.
21 G. De Falco, *et al.*, Electronic band gap of flame-formed carbon nanoparticles by scanning tunneling spectroscopy, *Proc. Combust. Inst.*, 2021, **38**(1), 1805–1812.
22 S. De, B. S. Satyanarayana and M. Srinivasulu, Band-gap measurement of room temperature grown clustered Carbon films for large area microelectronics, *J. Electron Devices*, 2014, **19**, 1601–1607.
23 H. Miqdad, Effect of Carbon Black Nanoparticles on the Optical Properties of poly (ethylene oxide) Films, *Int. J. Appl. Eng. Res.*, 2018, **13**(6), 4333–4341.
24 N. Elhalawany, A. M. Abdel-Karim and M. M. Saleeb, Preparation and evaluation of some nanocarbon (NC) based composites for optoelectronic applications, *Sci. Rep.*, 2023, **13**(1), 8987.
25 Ö. B. Mergen and E. Arda, Determination of optical band gap energies of CS/MWCNT bio-nanocomposites by Tauc and ASF methods, *Synth. Met.*, 2020, **269**, 116539.
26 K. K. Ahmed, *et al.*, A brief review on optical properties of polymer composites: insights into light-matter interaction from classical to quantum transport point of view, *Results Phys.*, 2024, **56**, 107239.
27 J. Piwowarczyk, *et al.*, XPS and FTIR studies of polytetrafluoroethylene thin films obtained by physical methods, *Polymers*, 2019, **11**(10), 1629.
28 S. B. Aziz, *et al.*, Characteristics of poly (Vinyl alcohol)(PVA) based composites integrated with green synthesized Al3+-metal complex: Structural, optical, and localized density of state analysis, *Polymers*, 2021, **13**(8), 1316.
29 B. C. Smith, The infrared spectra of polymers, VI: Polymers with CO bonds, *Spectroscopy*, 2022, **37**(5), 15–19.
30 W. Abd El-Fattah, *et al.*, Development of a PTFE membrane with photo-thermal activated carbon nanomaterials for improved solar-driven membrane distillation, *RSC Adv.*, 2025, **15**(49), 41946–41958.
31 H. T. Cairney, E. A. Hjelvik and A. P. Straub, Impact of Oxidative Chemicals on Hydrophobic Porous Membranes Used in Membrane Distillation, *ACS Appl. Eng. Mater.*, 2024, **2**(4), 1162–1169.
32 P.-Y. Hsu, *et al.*, Swelling-resistant, crosslinked polyvinyl alcohol membranes with high ZIF-8 nanofiller loadings as effective solid electrolytes for alkaline fuel cells, *Nanomaterials*, 2022, **12**(5), 865.
33 N. Q. Vu, *et al.*, Engineering functional PVA: A comprehensive review of chemical modifications and prospective developments, *ACS Polym. Au*, 2025, **6**(1), 33–60.
34 E. Rynkowska, *et al.*, Chemically and thermally crosslinked PVA-based membranes: effect on swelling and transport behavior, *Polymers*, 2019, **11**(11), 1799.
35 P. Piluso, *et al.*, Acetalization of poly (vinyl alcohol) by a fatty aldehyde in water medium: Model study, kinetics, and structure analysis, *J. Polym. Sci., Part A: Polym. Chem.*, 2018, **56**(6), 661–671.
36 A. Franken, *et al.*, Wetting criteria for the applicability of membrane distillation, *J. Membr. Sci.*, 1987, **33**(3), 315–328.
37 D. M. Warsinger, *et al.*, Scaling and fouling in membrane distillation for desalination applications: a review, *Desalination*, 2015, **356**, 294–313.
38 A. L. McGaughey, *et al.*, Hydrophobicity versus pore size: polymer coatings to improve membrane wetting resistance for membrane distillation, *ACS Appl. Polym. Mater.*, 2020, **2**(3), 1256–1267.
39 J. Cai, Z. Liu and F. Guo, Transport analysis of anti-wetting composite fibrous membranes for membrane distillation, *Membranes*, 2020, **11**(1), 14.
40 P. Woźniak and M. Gryta, Wettability Studies of Capillary PTFE Membranes Applied for Membrane Distillation, *Membranes*, 2023, **13**(1), 80.
41 H. A. Hijaz, *et al.*, Experimental investigation of temperature polarisation by capturing the temperature profile development over DCMD membranes, *J. Membr. Sci.*, 2023, **687**, 122089.
42 M. Suleman, M. Asif and S. A. Jamal, Temperature and concentration polarization in membrane distillation: A technical review, *Desalination Water Treat.*, 2021, **229**, 52–68.
43 L. Jing, *et al.*, Experimental Investigation of Temperature Polarization near Membrane Surface During Air Gap Membrane Distillation Processes, *Membranes*, 2025, **15**(6), 185.
44 M. Romeo, *et al.*, Self-Heating Graphene Oxide Composite Membranes for Desalination *via* Photothermal Membrane Distillation, *Adv. Funct. Mater.*, 2026, e29125.

45 M. Pagliero, *et al.*, Carbon black/polyvinylidene fluoride nanocomposite membranes for direct solar distillation, *Energies*, 2022, **15**(3), 740.
46 S. kumar Balu, *et al.*, Solar-driven interfacial evaporation: materials design and device assembly, *Energy Mater.*, 2024, **4**(2), 400021.
47 Y. Liu, *et al.*, Surface modification of dual-phase ceramic membrane reactor for coupling catalytic CO2 conversion with partial oxidation of methane, *J. Membr. Sci.*, 2024, **692**, 122312.
48 J. Zhang, *et al.*, Regulating lithium deposition *via* electropolymerization of acrylonitrile in rechargeable lithium metal batteries, *Nano Energy*, 2021, **88**, 106298.
49 Z. Chen, *et al.*, Separable Janus photothermal PPy@ PVA-PVDF/F-SiO2-PVDF bilayer membrane for low-cost, efficient and sustainable solar-driven membrane desalination in oil-contaminated seawater, *Chem. Eng. J.*, 2024, **496**, 153944.
50 J. Sun, *et al.*, MXene-PVA-TiO2-based photothermal-catalytic membrane with high structural stability for efficient desalination and photodegradation, *Chem. Eng. J.*, 2023, **468**, 143744.
51 Z. Chen, *et al.*, Separable Janus Photothermal Ppy@ Pva-Pvdf/F-Sio2-Pvdf Membrane for Low-Cost, Efficient and Sustainable Solar-Driven Membrane Desalination in Oil-Contaminated Seawater, *Chem. Eng. J.*, 2024, **496**, 153944.